Mechanism and Prediction of Laser Wet Cleaning of Marble Encrustation

Jie Zhang

Andrew J. Birnbaum

Y. Lawrence Yao

Department of Mechanical Engineering,
Columbia University,
New York, NY 10027

Fen Xu

John R. Lombardi

Department of Chemistry,
City College of New York,
New York, NY 10031

During the removal of encrustation from marble with 355 nm laser pulses, the effects of the thin liquid layer covering the encrustation are experimentally and numerically investigated. The working mechanism of the liquid layer is analyzed. A two-dimensional axial symmetric model is proposed to simulate the changes in the temperature, liquid volumetric fraction, and vapor pressure in the irradiated encrustation. To model the conservation of mass, momentum, and energy, three coupled nonlinear partial differential equations are numerically solved. The measured porosity of the encrustation is incorporated into the model. Marble cleaning with three different liquids having different thermodynamic properties, distilled water, ethanol, and acetone, are compared in terms of the cleaning efficiency at different fluence levels. With the liquid layer, the surface color of cleaned marble is also studied. In addition, surface-enhanced raman spectroscopy and a chromameter are used to identify the chemical constituents and measure the color of the cleaned marble, respectively. [DOI: 10.1115/1.2927446]

1 Introduction

Artifacts and buildings, made of natural stones such as marble, are inevitably and gradually covered by a thin layer of black encrustation. The black encrustation must be removed as it facilitates the degradation of the stone and also decreases the aesthetic value of the stone dramatically. At present, chemical cleaning and mechanical cleaning are widely used to remove the encrustation. Due to the possible environmental pollution and the strong dependence on the operator's techniques, the dominant status of chemical and mechanical cleaning is challenged by laser cleaning. Irradiated by the laser pulse, the encrustation can be ablated, but the stone remains intact after the removal of encrustation due to the large differences in their respective reflectivities. This characteristic, called "self-limiting," is very helpful in implementing safe and accurate stone cleaning.

Since Asmus in 1971 first proposed to apply a pulsed laser in cleaning encrustations from marble, the effectiveness of Nd:YAG (neodymium-doped yttrium aluminum garnet, Nd: $Y_3Al_5O_{12}$) laser in the restoration of various stoneworks has been implemented by the massive investigations [1]. However, there are some disadvantages. Pulsed lasers have not succeeded in removing very thick encrustations. Cleaning efficiency is relatively low due to the low ablation rates. The laser pulse induced elevated temperatures can lead to undesirable thermal side effects, such as redshift and vitrification, on the cleaned surface [2]. In addition, the stone surface displays severe yellowing after the cleaning with a laser at 1064 nm [3], and even the 355 nm laser pulse at low fluence leads to the yellowing of the stone [4].

Many efforts have been made to investigate the particular contamination removed from microelectronic parts with pulsed lasers. As the dimension of microelectronic parts is constantly shrinking, their tolerance to particle size also decreases. Laser steam cleaning has shown great potential in cleaning submicron-sized particles as the generated cleaning force is much larger than in dry cleaning. Kim et al. in 2004 investigated the physical mechanism of laser steam cleaning. It was proven that the cleaning force comes from bubble nucleation in the superheated liquid [5]. Lu et al. in 1998 proposed a model to calculate the cleaning force generated during the inertial-controlled bubble growth [6].

In the present paper, laser cleaning carried out right after a thin layer of suitable liquid is sprayed onto the encrustation is referred to as laser wet cleaning. A black encrustation approximately 500 μm thick was removed from limestone by a Q-switched Nd:YAG laser at 1064 nm with the assistance of distilled water. In the case of a thin encrustation approximately 50 μm thick on limestone, the cleaning rate with water was higher than that without water [7]. The application of water prevented the laser cleaned pliocene sandstone from any thermal side effect. It was speculated that the water significantly cooled down the irradiated volume because its specific heat is five times higher than sandstone [2]. The measured reflectivity of wet encrustation on sandstone was lower than that of dry encrustation. This may contribute to the increase in cleaning rate with water [8].

Cooper et al. in 1995 also found that cleaning efficiency was enhanced in laser wet cleaning of limestone in terms of the removed encrustation area due to the water penetration into the porous encrustation. During laser irradiation, the water in the pore would be explosively vaporized by the heat transferred from the encrustation, and generate large transitive forces exerting on particles within the encrustation. These forces were sufficient to loosen the encrustation, which was very beneficial to laser cleaning [9]. However, the working mechanism of water in laser cleaning is still not very clear, and no theoretical analysis has been performed.

In the present paper, the mechanism of laser wet cleaning is proposed. Coupled heat and (moisture) mass transport within the laser irradiated porous encrustation is used to model laser wet cleaning. The corresponding governing equations are numerically solved with finite element methods to calculate the distribution of temperature, pressure, and water volumetric fraction in the encrustation. The effects of distilled water, ethanol, and acetone on the cleaning efficiency of the encrustation from marble are compared experimentally and numerically. There is some agreement between the experimental and numerical values of the cleaning efficiency. Also, the color of marble surfaces cleaned by laser wet cleaning is analyzed.

2 Mechanism of Laser Wet Cleaning

In laser wet cleaning, the thin layer of liquid is sprayed onto the porous encrustation just prior to laser irradiation. Liquid penetrates and fills in the minute pores of the encrustation. When

Manuscript received January 12, 2007; final manuscript received November 19, 2007; published online May 23, 2008. Review conducted by Bin Wei.

laser irradiation starts, both the encrustation and liquid are heated. Once the temperature reaches the boiling point of liquid, it is vaporized immediately. Since liquid is vaporized at a rate much higher than its migration rate, vapor pressure is built up in the pore. If the pressure is larger than the reduced tensile strength of the encrustation at high temperature, the encrustation may be stripped away locally. The stripping in turn will accelerate the heat transfer in the encrustation and result in the new establishment of the pore pressure at the deeper level. Meanwhile, the ablation still plays a role in the removal of encrustation.

2.1 Mathematic Modeling. During laser wet cleaning, laser pulses induce the evaporation of liquid and the subsequent built-up pressure in the pore. Driven by the pressure gradient, the liquid and the vapor are convected among the encrustation pores, which affect the heat transfer in the encrustation. Gypsum ($CaSO_4 \cdot 2H_2O$), the major encrustation ingredient, contains 21% chemically bound water by weight. Chemically bound water is released into the pore at 373 and 573 K, respectively [10]. The absorbed laser heat is partly transferred into the encrustation by the liquid, vapor and encrustation together, partly absorbed by the evaporation of liquid and partly consumed by the gypsum dehydration. Accordingly, coupled heat transfer and mass transport determines the temperature and pressure distribution within the encrustation.

Coupled heat and mass transport in the porous encrustation is based on the averaging of the quantities over a representative elementary volume (REV) [11]. The volumetric fraction of each phase composing a REV with volume V is defined as

$$\varepsilon_i = \frac{V_i}{V}, \quad i = s,l,g \tag{1}$$

where the subscripts s, l, and g indicate the solid, liquid, and gas, and V_i is the phase i volume. The sum of the volumetric fractions of three phases is equal to 1. It is assumed that the porous encrustation is full of liquid before the irradiation. The encrustation porosity ε is calculated as $\varepsilon=\varepsilon_l+\varepsilon_g$ and $\varepsilon_s=1-\varepsilon$.

The following assumptions are applied: (a) The liquid is incompressible, ρ_l=const. (b) Compared to the gas, the mobility of the liquid is negligible [12]. (c) No dry air stays in the pore. (d) The vapor phase is only liquid vapor and the vapor is an ideal gas. (e) The encrustation is homogeneous and isotropic. (f) Local thermodynamic equilibrium is achieved. (g) Except dehydration of the gypsum, no other thermochemical reactions occur.

The mass conservation equation of gas is

$$\frac{\partial}{\partial t}(\rho_g \varepsilon_g) = -\nabla \cdot (\rho_g V_g) + \Gamma \tag{2}$$

where V_g is the gas velocity determined with Darcy's law as follows:

$$V = -\nabla \cdot \left(\frac{K}{\nu} P\right) \tag{3}$$

where K and ν are the permeability and dynamic viscosity of the vapor, and P is the pore pressure. Vapor density ρ_g is calculated with the Dalton equation, $\rho_g=MP/RT$, where R is the universal gas constant, M is the molar weight of vapor, and T is the temperature. Γ is the evaporation rate of liquid.

Based on the enthalpy balance, the heat conduction and convection in the encrustation are governed by

$$\rho C_p \frac{\partial T}{\partial t} + \rho_g \varepsilon_g C_{pg} V \nabla T = \nabla \cdot (k \nabla T) \tag{4}$$

where t is the time, and ρC_p is the effective heat capacity for the porous encrustation, calculated as $\rho C_p=(1-\varepsilon)\rho_s(C_{ps}+E\Delta h_d)+\varepsilon_l\rho_l(C_{pl}+F\Delta h)+\varepsilon_g\rho_g(C_{pg}+F\Delta h)$, where ρ_i and C_{pi} are density and specific heat of the corresponding phases, respectively [13]. Δh_d and Δh are the reaction heat of gypsum dehydration and the latent heat of the liquid vaporization, respectively. E and F are the derivative of solid and liquid phase volumetric fraction variation with temperature, respectively. The effective thermal conductivity for the porous encrustation k is defined as $k=(1-\varepsilon)k_s+\varepsilon_l k_l+\varepsilon_g k_g$ [14].

Only if the evaporation rate of liquid Γ is known, the temperature, pore pressure, and liquid volumetric fraction can be solved from Eqs. (2) and (4). In most coupled heat and mass transport models, a set of sorption isotherms is adopted to describe the dependence of water evaporation on temperature and pressure [12,15,16]. The accurate sorption isotherms are rather difficult to measure. Therefore, the evaporation rate of liquid is assumed to be related to the ratio of the vapor pressure to the saturated pressure at the corresponding temperature in some models [17,18]. However, such a definition makes the accuracy of evaporation rate heavily reliant on the estimated evaporation rate constant. In the present paper, considering the laser pulse to be strongly instantaneous, the vapor volumetric faction is defined as

$$\varepsilon_g = \varepsilon U(T - T_{\text{trans}}, \Delta T) \tag{5}$$

where U is a step function whose value is zero at $T \le T_{\text{trans}}-\Delta T$, is equal to 1 at $T \ge T_{\text{trans}}+\Delta T$, and is uniformly distributed in the range from $T-T_{\text{trans}}$ to $T+T_{\text{trans}}$ [13]. Therefore, one obtains $\varepsilon_l=\varepsilon-\varepsilon_g$ and $F=U(T-T_{\text{trans}},\Delta T)/dT$.

The encrustation porosity ε varies with the dehydration of gypsum as

$$\varepsilon = \varepsilon_0 + \frac{\rho_{\text{water}} \delta_{sw}}{\rho_s} \tag{6}$$

where ε_0 is initial porosity, the effective density of water ρ_{water} is 21% of water density, δ_{sw} is the released water fraction, defined as $\delta_{sw}=\xi U(T-T_{\text{trans}},\Delta T)$, where U is also a step function, and coefficient ζ is equal to 0.75 and 0.25 at T_{trans} of 373 and 573 K, respectively. The encrustation density ρ_s is equal to $\rho_s=\rho_{s0}-\rho_{\text{water}}\delta_{sw}$, where ρ_{s0} is the initial encrustation density.

The initial conditions are assumed to be T=300 K, P=101 325 Pa=1 atm, $\varepsilon_l=\varepsilon$, and $\varepsilon_g=0$. On the laser-irradiated surface, the boundary condition is specified as $-K\nabla T\cdot\mathbf{n}=I+h(T-T_\infty)$, P=101 325 Pa=1 atm, $\varepsilon_l=0$ and $\varepsilon_g=\varepsilon$, where $\mathbf{n}$ is the outward unit vector of the surface, the heat transfer coefficient h is $h=h_c+\sigma e(T+T_\infty)(T^2+T_\infty^2)$, h_c is the convective heat transfer coefficient, σ is the Stefan–Boltzmann constant, e is the emissivity, and T_∞ is the environment temperature of 300 K. I is the absorbed laser fluence, calculated as $I=\alpha I_0 \exp(-r^2/b^2)$, where α is the surface absorptivity, I_0 is the incident fluence, b is the beam radius, and r is the distance of the irradiated point to the beam center located at the symmetrical axis. On the non-laser-irradiated surface, the boundary conditions are applied, T=300 K, P=101 325 Pa=1 atm, $\varepsilon_l=0$, and $\varepsilon_g=\varepsilon$.

2.2 Numerical Analysis. The coupled partial differential equations (PDEs) (2) and (4) with boundary and initial conditions are solved through finite element methods. FEMLAB 3.2 software is used. A two-dimensional axial symmetrical model with the dimension of 200×120 μm^2 is established. The mapped mesh with two-directional bias is created in the model, shown in Fig. 1. The application modes of transient conduction and convection, as well as Darcy's law in chemical engineering module, are adopted.

In the model, a smoothed Heavyside function with a continuous second derivative, flc2hs, is chosen as the step function U. In the case of vaporized liquid (vapor), T_{trans} are set as 423 K, 401 K, and 379 K for water, ethanol, and acetone, respectively, and ΔT is 50 K. It is assumed that the water vaporizes starting from 373 K and all of water is vaporized at 473 K well below the critical point of water, 647 K, because laser heating is extremely strong and fast. Similarly, the evaporation of ethanol and acetone is assumed to take place within the range from 351 K to 451 K and from

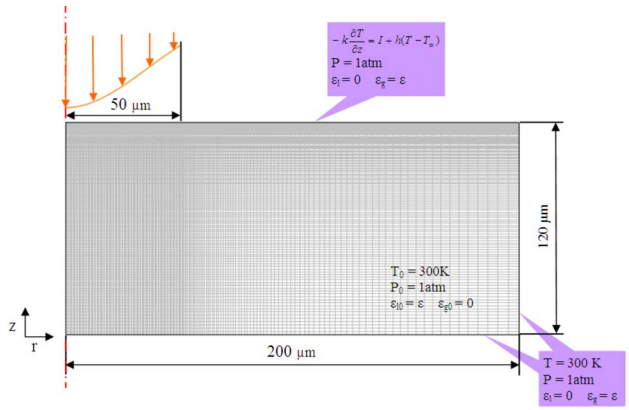

Fig. 1 Schematic of the established model for laser wet cleaning

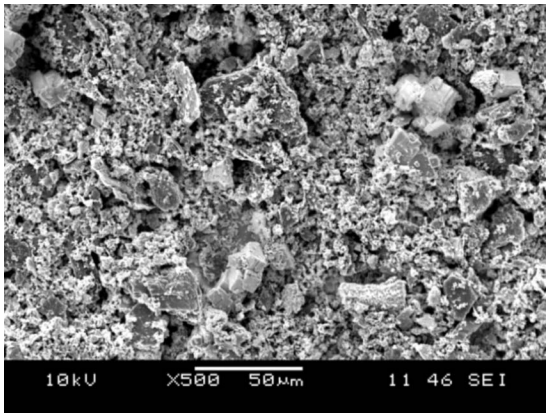

Fig. 2 SEM image of the artificial encrustation on marble

329 K to 429 K, respectively. Concerning gypsum dehydration, T_{trans} is set as 398 K and 598 K for two dehydration reactions, respectively, and ΔT is 25 K.

Due to the constraint of the software, the laser-ablated part cannot be removed from the calculation domain. To decrease its effect on the calculation results, the thermal conductivity in the ablated element is assumed to be 5000 W m^{-1} K^{-1} once this element temperature is larger than the evaporation point.

All thermodynamic data of liquids come from Ref. [19]. The specific heat and dynamic viscosity of ethanol and acetone vapor are calculated by the method of Joback and the method of Chung, respectively, [19]. In Ref. [20], the permeability of unfractured metamorphic rock ranges from 10^{-18} to 10^{-20}. Marble belongs to metamorphic rock. However, the marble encrustation is mainly constituted by softer and water-soluble gypsum, so the porosity of encrustation becomes larger. The permeability of the encrustation is assumed to decrease to 1×10^{-12}.

3 Experimental Conditions and Material Characterizations

The studied sample is Italian white Carrara marble with a honed surface. The sample is a cubic 15 mm long, 15 mm wide, and 9 mm thick. With the concern of numerical calculation accuracy, the marble is covered with the artificial encrustation, a compound of 5% hematite (Fe_2O_3) powder, 20% graphite powder, and 75% gypsum (vol. %). The average encrustation thickness is approximately 120 μm. The formation method of the encrustation is introduced in detail in Ref. [4].

Laser wet cleaning is performed with a Q-switched Nd:YAG laser at 355 nm in open air. The pulse duration is 50 ns. Other technical specifications for the laser are given in Ref. [4]. All cleaning experiments were conducted with a laser beam with the diameter of 100 μm. A thin layer of liquid is sprayed onto the encrustation every 2 s to assure the encrustation is wet. The compressed air is always blowing onto the focusing lens during cleaning. Thus, the focusing lens is protected from the attachment of ablated particles, and the wet encrustation cannot be blown dry.

The scanning electron image (SEM) image of the encrustation presented in Fig. 2 reveals that the artificial encrustation is a porous structure. Porosity measurement is based on Archimedes' principle. The mixture including the same ingredients as the artificial encrustation is brushed onto the bottom of a 60 mm dish layer by layer, until reaching the thickness of 2.5 mm. This dish with the sample is weighed with a digital balance. Distilled water is then poured onto the sample surface very slowly to make sure the water fills in all the fine pores in the sample. The dish with the sample full of water is weighed again. Since the density of water is close to 1 kg/m^3, the ratio of the weight difference to the known sample volume is equal to the porosity of the sample.

A chromameter (Minolta CR-300) and surface enhanced Raman spectroscopy are employed to measure the surface color and constituents. Their detailed introductions are in Ref. [4]. SEM is used to take the image for the encrustation coated with silver.

4 Results and Discussions

4.1 Effect of Distilled Water on the Cleaning Efficiency

4.1.1 Experiments. In the present paper, the cleaning efficiency is denoted as the weight of the encrustation removed by one single pulse. To increase the weight variation of the cleaned sample between pre- and post-laser cleaning, a thin layer of encrustation in two circular areas with the diameter of 5 mm is removed. The laser pulses irradiate the encrustation along the circular orbits from the outside to the inside. The pulses have an overlapping rate of 50% to reduce the effect of the Gaussian beam. At the specified beam center locations, only one single pulse is deposited onto the encrustation. After two circular areas are irradiated once, the samples are weighed and compared with the initial weights. The sample weight difference divided by the number of deposited pulses, namely, 16002, is equal to the ablated encrustation weight by one single pulse. In laser wet cleaning, the cleaned samples are not weighed after being dried.

Considering the ablation thresholds of encrustation and marble at 355 nm, 0.45 J/cm^2 and 2.5 J/cm^2, respectively [4], laser fluences of 0.49 J/cm^2, 0.67 J/cm^2, 0.95 J/cm^2, 1.3 J/cm^2, and 1.45 J/cm^2 are applied to ablate the encrustation without or with distilled water. The corresponding ablated encrustation weights by one single pulse are compared in Fig. 3. Obviously, the use of water enhances the cleaning efficiency at every fluence level. White paper is put around the work stage during experiments to collect the encrustation debris. Some debris shown in Fig. 4 ranges approximately from 100 to 200 μm. This rather large debris is most likely produced by the encrustation stripping due to the vapor pressure.

In addition, Fig. 3 indicates the increase in cleaning efficiency with the distilled water as the fluence level increases. The possible reason is that the high fluence leads to high temperature and much stronger pressure. Moreover, the water in the deeper pores can be heated by the high fluence, so the vapor pressure may be established there as well.

4.1.2 Simulated Distribution of Temperature, Pressure, and Water Volumetric Fraction Within the Irradiated Encrustation. Assume that one single pulse at different fluence irradiates the encrustation. On average, the measured porosity of the encrustation is approximately 0.475.

Figure 5 shows the surface contours of temperature, water volu-

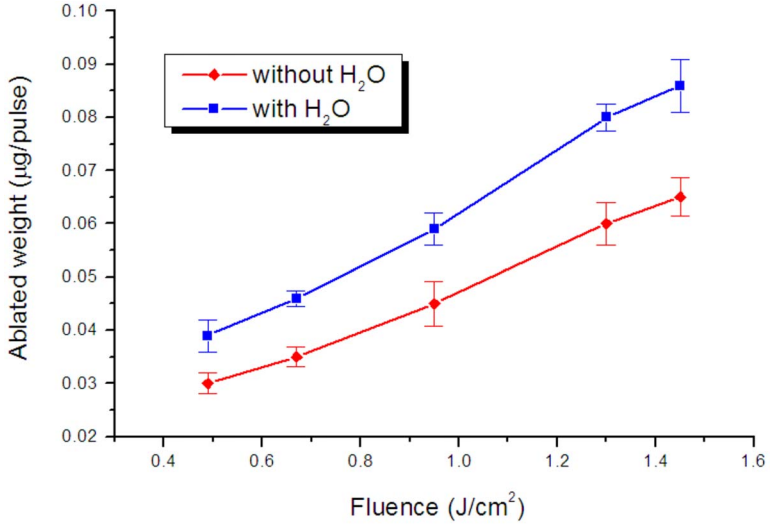

Fig. 3 Comparison of the ablated encrustation weight by one single pulse at different fluence levels without and with distilled water

metric fraction, and pressure at 50 ns produced by the pulse at 0.67 J/cm^2 in the partial irradiated encrustation (10×98 μm^2). In the temperature contour, the red arrows denote the total heat flux. The two isotherm lines correspond to 2160 K and 373 K, respectively. The isotherm line of 2160 K is at the very shallow location, which means very little of the encrustation is thermally ablated. The isotherm line of 373 K indicates that the water in the pores about 2.5 μm below the irradiated surface starts to vaporize. The distribution of water volumetric fraction agrees with the temperature contour. At temperatures below 373 K, water fills in the pore, and the water volumetric fraction equals to the porosity of 0.475. At temperature above 373 K, all of water is vaporized in the majority of the area. The evaporation only exists in the very small area.

The pressure contour shows the pressure is built up in the area at temperature above 373 K, encircled by the isotherm line of 373 K. In the area without water vaporization, the pressure is still equal to 1 atm. The maximal pressure is marked. Obviously, its location is very near the start line of water vaporization. The pressure gradually decreases from the deep to the shallow area, which drives the water vapor to flow toward the encrustation surface and escape into the air. In addition, the maximal pressure approaches over 7.7 atm. Since the encrustation is artificially made, its tensile strength is assumed to be very low, approximately 3–4 atm. Accordingly, the maximal pressure may be large enough to spall the encrustation off.

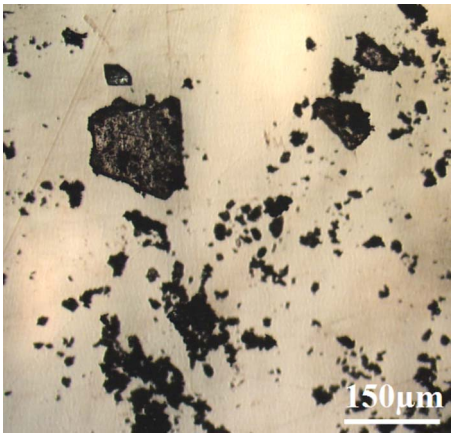

Fig. 4 Images of debris collected during laser wet cleaning experiment

The time history of temperature, pressure, and water volumetric fraction at the point with the maximal pressure at 50 ns is shown in Fig. 6. In the first 20 s, the absorbed laser heat is not transferred to this point, and has a negligible effect on its temperature. This point is heated within the following 30 s of the pulse duration. However, after 50 ns, its temperature continues to rise due to the heat transferred from the top area with high temperature. Below 373 K, the water volumetric fraction is equal to the porosity. Once the temperature reaches 373 K, the water volumetric fraction increases slightly due to the compromise of the vaporized water and the released water from the gypsum dehydration. Then, after the completion of the gypsum dehydration, the variation of water volumetric fraction only reflects the extent of water vaporization. At 473 K, all of the water is vaporized.

The pressure starts to build up at 373 K. The peak value of pressure is located at the interface between the dry and wet encrustations with the temperature of 475 K. In addition, the pressure increases with the temperature during laser irradiation. The temperature still increases after the laser irradiation, yet the pressure decreases. In the former case, the increase in pressure is attributed to the vaporization of more and more water. In the latter case, the limited pressure increase resulting from the slow heating cannot compensate the pressure decrease caused by the strong gas movement upward to the surface.

Figure 7 shows the time history of temperature and pressure at two points along the symmetrical axis with the depths of 0.1 and 1 μm, respectively. In Fig. 7(*a*), the point at the depth of 0.1 μm (z=119.9 μm) is heated up to 2160 K at approximately 35 ns. After 35 ns, its temperature fluctuates around 2160 K, which means this point is within the area that is thermally ablated. Concerning the point at the depth of 1 μm (z=119 μm), its temperature increase starts at about 7 ns and continues until 50 ns. After the end of pulse irradiation at 50 ns, its temperature continues to increase due to the heat transferred from the adjacent area of higher temperature, and then decreases. The model described in Ref. [4] is adopted to calculate the temperature produced at the same fluence as 0.67 J/cm^2 without the assistance of water. The corresponding temperature history at these two points is also shown in Fig. 7(*a*). It is observed that the temperature produced without water is higher than that produced with water, demonstrating water with a high specific heat cools the encrustation.

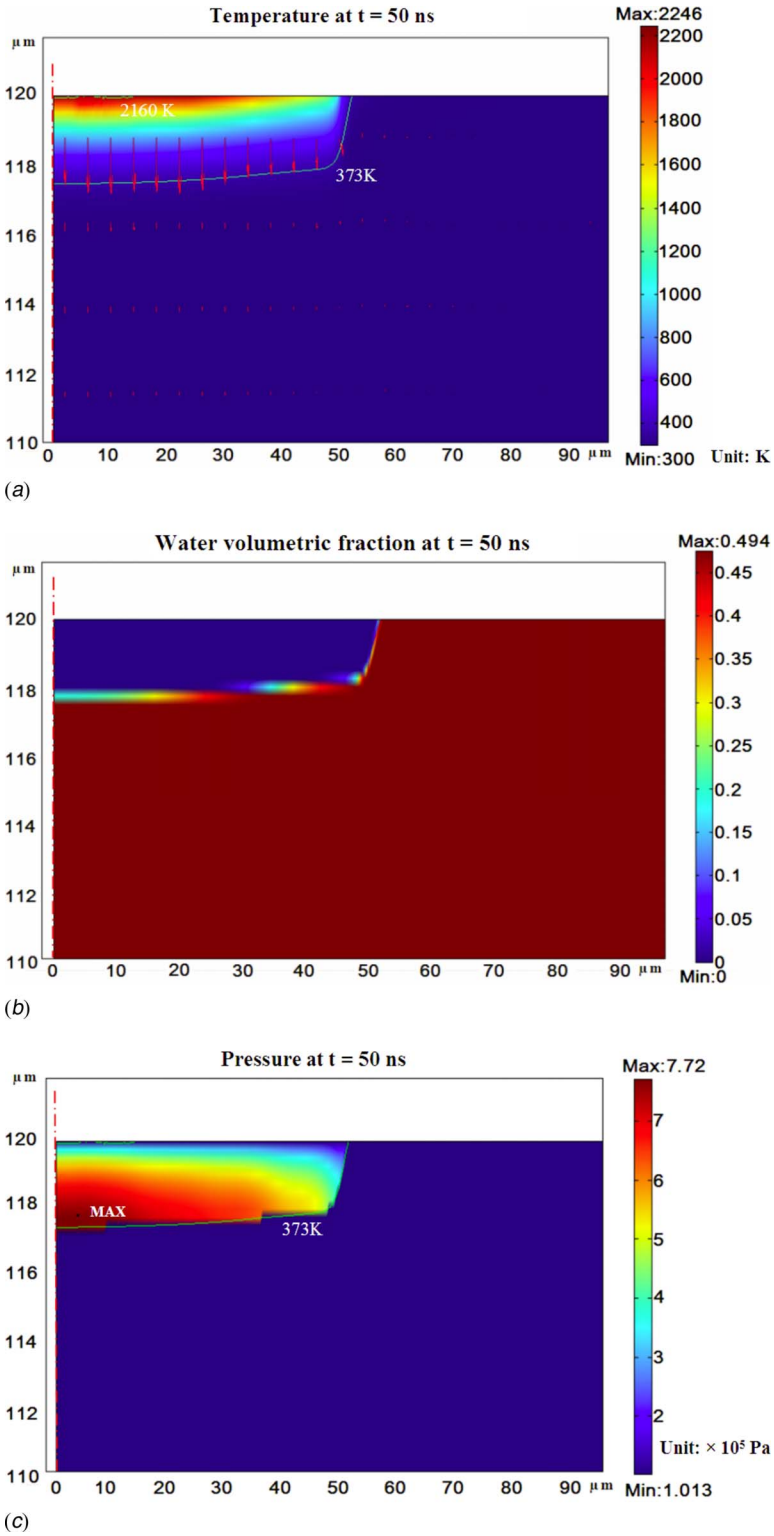

Fig. 5 Surface contours of (*a*) temperature with total heat flux, (*b*) water volumetric fraction, and (*c*) pressure at 50 ns produced by the pulse at 0.67 J/cm^2 in the partial encrustation (10×98 μm^2)

In Fig. 7(*b*), both pressures at the two points are established at 373 K. The peak pressures of the points at 119 μm and 119.9 μm appear at 526 K and 815 K, respectively. Below 526 and 815 K, the pressure increases continuously. Above 526 K and 815 K, the pressure gradually decreases.

The history of the velocities at the depth and radial direction of the point at z=119 μm is presented in Fig. 8. The radial velocity is much smaller than the velocity in the depth direction. It can be reasoned that the convection of water vapor along the depth direction is much more intense due to the enormous pressure gradient along this direction. As vaporization starts, the negative vapor velocity in the depth direction represents the vapor moves down-

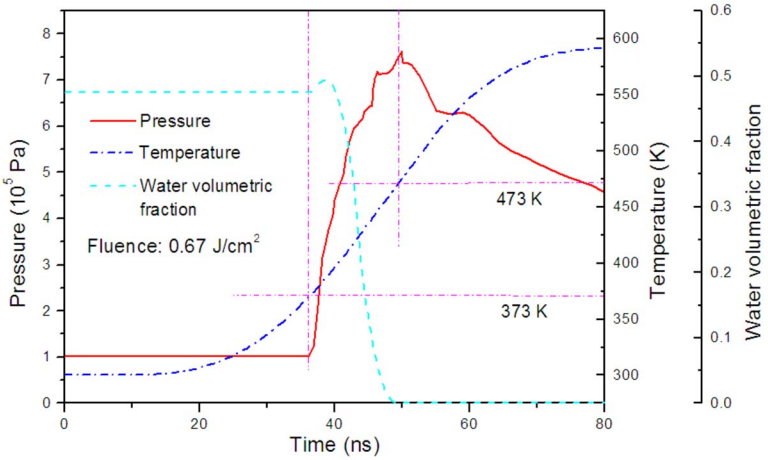

Fig. 6 Simulated time history of temperature, pressure and water volumetric fraction at the point with the maximal pressure at 50 ns in the encrustation irradiated at 0.67 J/cm^2

ward due to its pressure lower than the pressure of the upper nodes. Then, until 526 K or 815 K, the positive velocity means the vapor moves upward from the liquid surface and is accumulated in the pore. After that, the vapor starts to move out of the pore and toward the irradiated surface, which is verified by the positive velocity and the decreasing pressure.

The vapor, which escaped from the deeper pores, enhances the local pressure. On the other hand, the exiting of vapor further

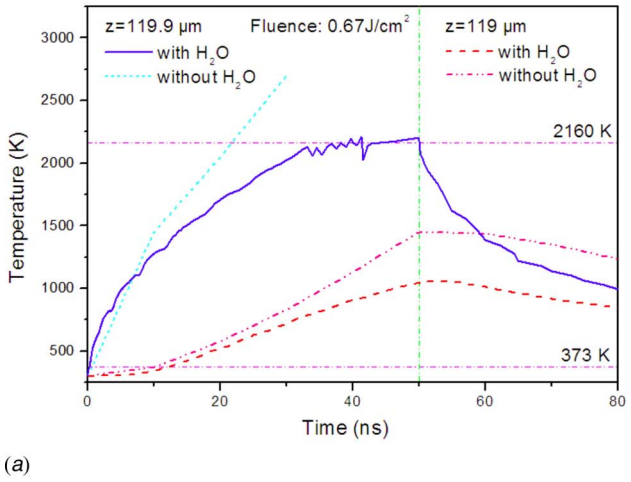

(*a*)

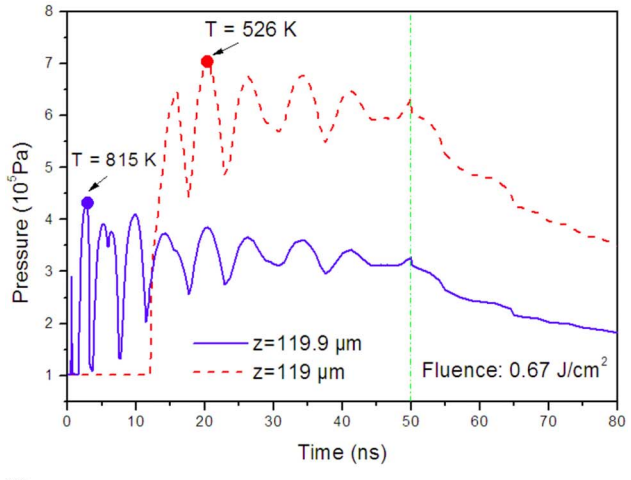

(*b*)

Fig. 7 Simulated time history of (*a*) temperature and (*b*) pressure of two points at the symmetrical axis produced by the pulse at 0.67 J/cm^2

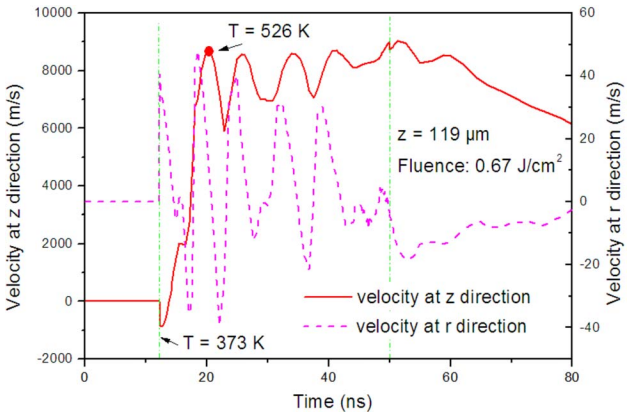

Fig. 8 Simulated time history of vapor velocity of the point at the symmetrical axis (z=119 μm) produced by the pulse at 0.67 J/cm^2

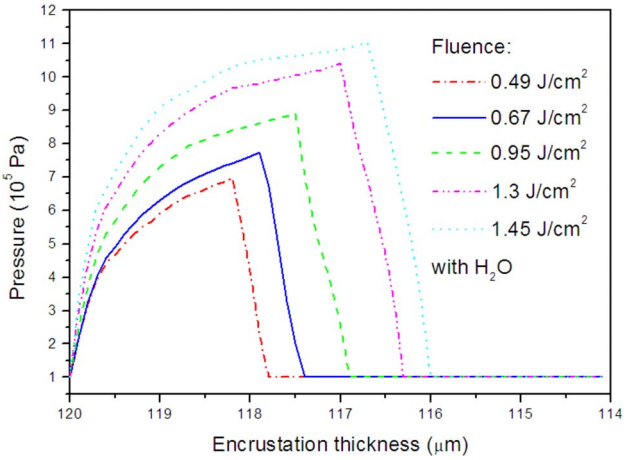

Fig. 9 Comparison of the pressure profiles along the symmetrical axis at 50 ns produced by the different fluences

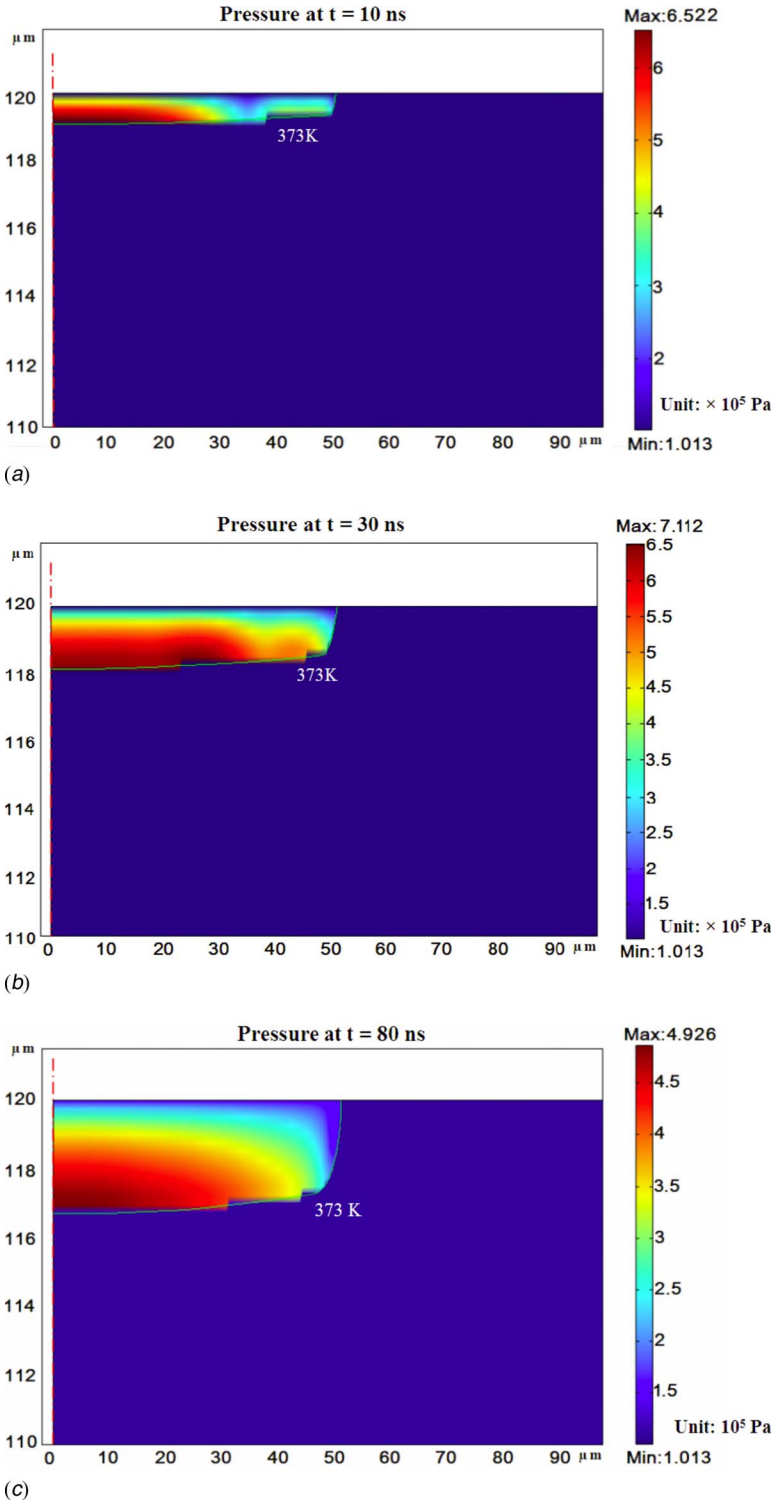

Fig. 10 Surface contours of pressure at (*a*) 10 ns, (*b*) 30 ns, and (c) 80 ns produced by the pulse at 0.67 J/cm^2 in the partial encrustation (10 $\times$98 μm^2)

reduces the local pressure. Accordingly, the local pressure fluctuates and also leads to fluctuation of the velocity. However, the velocity fluctuates around a constant value. This is because the fluctuating pressure decreases but the pressure gradient remains constant. There is a noticeable fluctuation occurring as the pressure increases, as shown in Fig. 7(*b*). However, the velocity does not follow this pattern. A possible explanation is that the lower pressure is built up during the initial water evaporation at a deeper level, and as a result the partial vapor flowing downward causes the pressure to fluctuate.

Table 1 Color measurements (ΔL^*, lightness; Δa^*, red-green; Δb^*, blue-yellow)

	Original marble	Encrustation	Marble cleaned by eight pulses at 0.67 J/cm^2	Original marble	Encrustation	Marble cleaned by six pulses at 0.67 J/cm^2 with water
ΔL^*	90.8433	59.3900	84.2767	84.9433	59.3900	82.8167
Δa^*	−1.0333	11.2167	−0.2033	−1.1427	11.2167	−0.0282
Δb^*	−0.9400	13.9633	1.8933	−0.7917	13.9633	−0.0690
	Original marble	Encrustation	Marble cleaned by five pulses at 0.67 J/cm^2 with ethanol	Original marble	Encrustation	Marble cleaned by five pulses at 0.67 J/cm^2 with acetone
ΔL^*	85.1453	56.2100	83.1182	87.0710	56.2100	84.0112
Δa^*	−0.9895	10.5608	−0.0531	−1.1621	10.5608	−0.0451
Δb^*	−1.0920	8.9632	−0.0484	−1.1217	8.9632	−0.0715

It can be seen in Fig. 7(*b*) that the pressure at 119 μm is always higher than that at 119.9 μm. The vapor at the shallow depth escapes easily, and thus the pressure is hard to be built up. The opposite is true for the deeper points.

4.1.3 Calculation of the Ablated Encrustation Weight by One Single Pulse. The pressure profiles along the symmetrical axis produced at fluences of 0.49, 0.67, 0.95, 1.3, and 1.45 J/cm^2 at 50 ns are shown in Fig. 9. The pressure field extends with fluence. The higher the fluence is applied, the larger the heat-affected zone is generated. Therefore, more water reaches the boiling point, and then the pressure is built up in a larger region. The induced maximal pressure increases with fluence as well. At high fluence, the water is vaporized much more quickly due to the high heating rate. Thus, the intensified amassment of the vapor promotes an increase in pressure.

The pressure contours produced at 0.67 J/cm^2 at 10 ns, 30 ns, and 80 ns are shown in Fig. 10. It can be seen that the maximal pressures at 10 ns, 30 ns, 50 ns, and 80 ns are about 6.5 atm, 7.1 atm, 7.7 atm, and 4.9 atm, respectively. The maximal pressure appears at 50 ns during laser wet cleaning. The increase in pressure with heating time results from vapor formed at deeper level being trapped and not being allowed to escape through pores. At 80 ns, the heat transferred from the above hot area still can vaporize the water, yet the generated pressure is relatively low due to the slow heating rate.

Suppose that once the maximal pressure at 50 ns exceeds the tensile strength, the whole encrustation with the diameter of 100 μm above the point with maximal pressure is completely removed. Accordingly, the ablated encrustation weight per pulse can be predicted. The experimental and simulated ablated encrustation weights by one single pulse are compared in Fig. 11. The simulated values have the same trend as the experimental values. Also, the former is rather close to the latter. Therefore, the proposed model is validated by the experiments to some extent.

The discrepancy between the simulated and experimental ablated weights is due to the shortcoming of the present model. In reality, a thin layer of encrustation may be stripped away at 10 ns due to the high pressure. Then, the laser beam irradiates the newly exposed surface and establishes the pressure again. However, the present model cannot exclude the removed part from the calculation domain. The discrepancy is aggravated with the fluence, which further reflects the inappropriate treatment of the pressure-removed part because the enhanced pressure by the fluence plays a more important role. Future research will improve the model in this aspect.

4.2 Effect of Other Liquids on the Cleaning Efficiency. Liquids with thermodynamic properties different from that of water have a different effect on the laser cleaning process. Ethanol and acetone are applied to assist the laser ablative cleaning. Both have very similar thermodynamic properties except that the boiling point and vaporization heat of ethanol are higher than that of acetone. However, their boiling point, specific heat, thermal conductivity, and vaporization heat are lower than that of water.

To rather accurately determine the cleaning efficiency, the experimental strategy described in Sec. 6.1.1 is followed. Laser cleaning with ethanol or acetone is performed at fluences of 0.49 J/cm^2, 0.67 J/cm^2, 0.95 J/cm^2, 1.3 J/cm^2, and 1.45 J/cm^2, respectively. The ablated encrustation weight by one single pulse with distilled water, ethanol, and acetone are compared in Fig. 12.

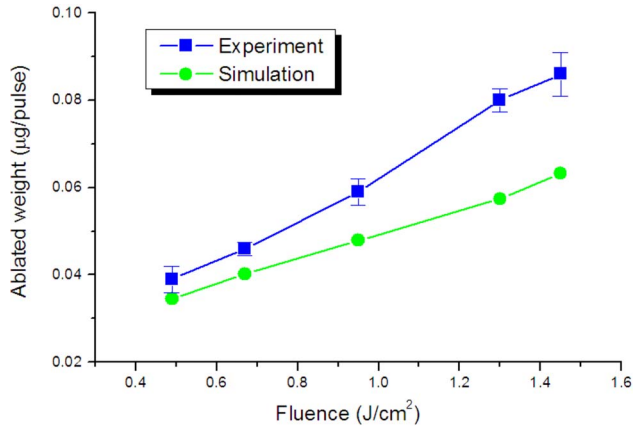

Fig. 11 Comparison of the experimental and simulated ablated encrustation weight by one single pulse at different fluence levels with distilled water

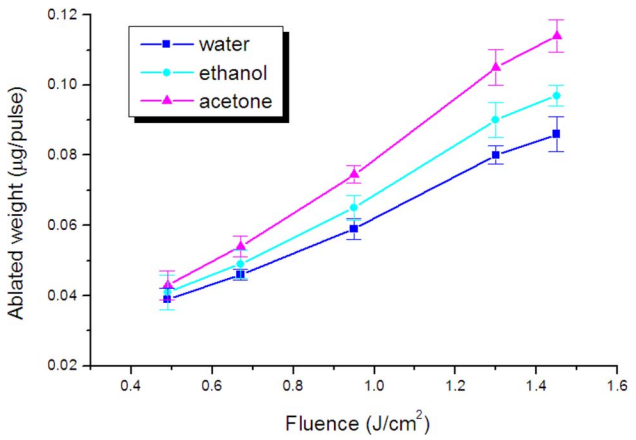

Fig. 12 Comparison of the ablated encrustation weight by one single pulse at different fluence levels with different liquids

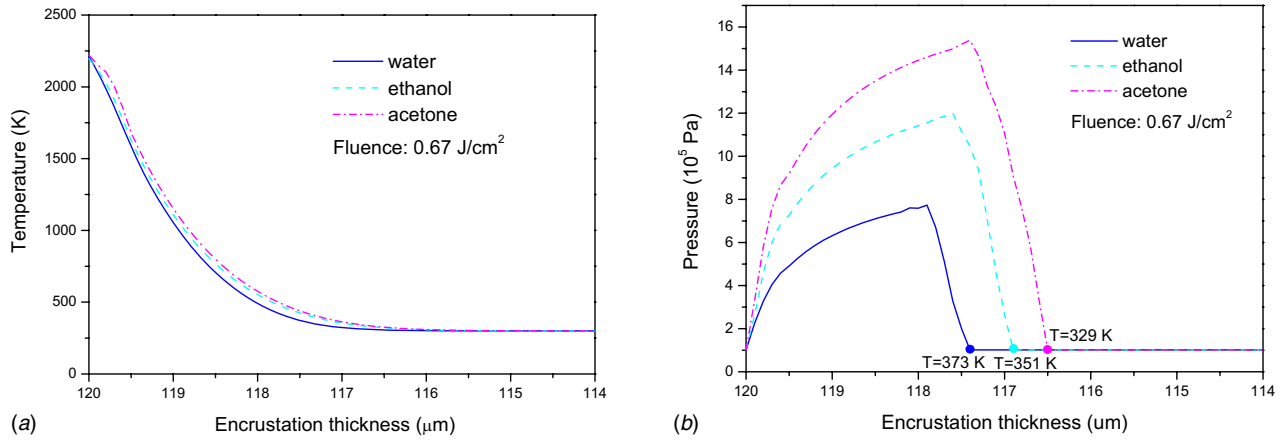

Fig. 13 Comparison of (*a*) temperature and (*b*) pressure profiles along the symmetrical axis at 50 ns with the pulse at 0.67 J/cm^2 with different liquids

At the same fluence, the ablated weight with acetone is the largest, that with distilled water is the smallest, and that with ethanol is in the middle. Though the ablated weight is enhanced with the fluence in all three cases, the increase in the ablated weight with acetone, ethanol, and water are in the order of decreasing value.

The likely reasons for the enhanced cleaning efficiency of acetone are now explained. The simulated pressure profiles along the symmetrical axis produced at 0.67 J/cm^2 with distilled water, ethanol, or acetone at 50 ns are compared in Fig. 13. Obviously, the vapor pressure is built up in the deepest and widest area in the case of acetone. Its low thermodynamic properties lead to heat being transferred further and faster. Thus, acetone is vaporized in many more pores. In addition, the peak value of the pressure induced by acetone is largest partially due to the higher heating rate.

4.3 Effect of Liquids on the Color of Cleaned Surface. To measure the surface color of cleaned marble, a circular encrustation with a diameter of 9 mm is removed to fit the 8 mm measurement spot of the chromameter. The method for removing the circular encrustation is described in Sec. 6.1.1. Zhang et al. in 2007 found that the marble surface became slightly yellowed after cleaning with the 355 nm pulse at 0.67 J/cm^2 [4]. For the comparative analysis, a fluence of 0.67 J/cm^2 is applied to clean marble with liquids. The encrustation is completely removed by eight pulses without liquids, six pulses with distilled water, five pulses with ethanol, and five pulses with acetone, respectively. This also reflects the improvement in the cleaning efficiency of wet cleaning.

The color measurements of the original and cleaned marble surface as well as the encrustation are listed in Table 1. All color data are the average of five independent measurements. Figure 14 shows the lightness (ΔL^*) and blue-yellow (Δb^*) coordinates in the 1971 CIE $L^*a^*b^*$ color space. Concerning the encrustation, the lower lightness denotes the black appearance of the encrustation due to the graphite. The positive Δa^* and Δb^* reflect that the encrustation color is inclined to the redness and yellowness due to the dark-brown hematite in the encrustation.

Four cleaned marble surfaces are very close to the original ones in the lightness, which implies the removal of the encrustation. The lightness difference between a marble surface cleaned with liquids and the original surfaces is less than that between the surface cleaned without liquids and its original surface. This means the encrustation may be completely removed in the former case. Without liquids, Δa^* of the cleaned surface is close to the original value and has the same sign. Yet, Δb^* of the cleaned surface is positive, which indicates that the surface becomes slightly yellowed. With liquids, both Δa^* and Δb^* of the cleaned surfaces are close to the original values and have the same sign. It can be concluded that there is no discoloration on the surfaces cleaned at low fluence with liquids.

The Raman spectra obtained on four cleaned surfaces at 514 nm are presented in Fig. 15. The spectrum of the surface cleaned without liquids consists of bands of $CaCO_3$ at 158 cm^{-1}, 285 cm^{-1}, 711 cm^{-1}, 1084 cm^{-1} [21] and bands of Fe_2O_3 at 224 cm^{-1} and 405 cm^{-1} [22]. Yet, the spectra of the surface cleaned with liquids only have the bands of $CaCO_3$. The $CaCO_3$ bands in four spectra indicate that the marble surfaces are exposed after the removal of the encrustation. The Fe_2O_3 bands reflect Fe_2O_3 still resides on the surface cleaned without liquids, and is responsible for the slightly yellowed surface.

In laser wet cleaning, since liquids consume the laser heat absorbed by the encrustation to raise the temperature and vaporize, the entire temperature field is decreased in the irradiated encrustation. This inhibits the reduction of hematite by the graphite. In addition, the majority of the encrustation is stripped away by the vapor pressure. The maximal vapor pressure takes place at the interface between the dry and wet encrustations, which is much lower than the ablation front in the encrustation. The stripping of the encrustation by the vapor pressure starts very near the interface. Even if some hematite is reduced to iron, the iron can be

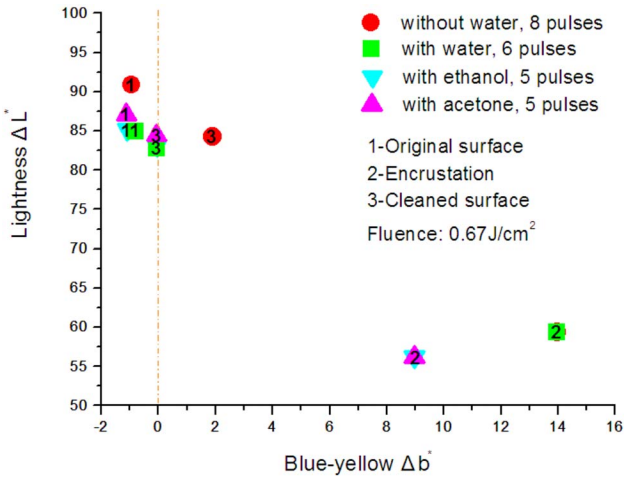

Fig. 14 The variation of two color coordinates of marble surface cleaned at 0.67 J/cm^2 without or with different liquids

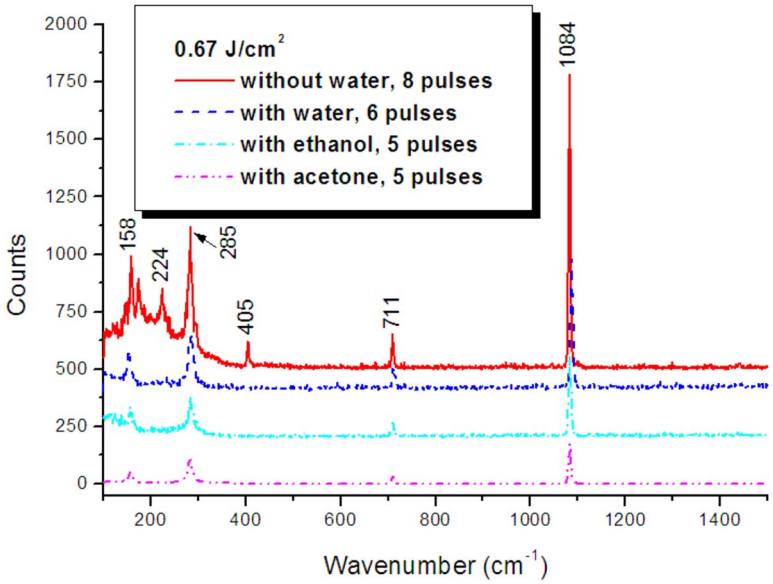

Fig. 15 Raman spectra collected from marble surface cleaned at 0.67 J/cm² without or with different liquids (Raman shifts are activated by the 514 nm cw laser at a power of 20 mW, the red, blue, and cyan lines have upward shifts of 500, 400, and 200 for the clarity, respectively)

taken away by the stripped encrustation. Thus, there is no possibility that the iron is left on the marble surface and then is oxidized by air after the laser irradiation.

5 Conclusions

The enhanced cleaning efficiency of laser wet cleaning, in the case of the stone encrustation, is due to the generation of vapor pressure. The liquid in the encrustation pores is vaporized, and the accumulated vapor induces a build up of pressure. Once the pore pressure exceeds the tensile strength of the encrustation, the encrustation is stripped away. The established model describing coupled heat transfer and mass transport in the porous structure can simulate the distribution of temperature, vapor pressure, and liquid volumetric fraction in the encrustation produced by the laser irradiation. The model-predicted ablated encrustation weight by one single pulse agrees with the experimental values to some extent. The difference in the cleaning efficiency between laser wet and dry cleaning increases with the incident fluence. The use of liquids with low boiling points and specific heats in laser wet cleaning is more beneficial to boost the cleaning efficiency. With the assistance of liquids, no discoloration occurs on the surface cleaned by the 355 nm pulse with the low fluence. The iron from the reduction of hematite by graphite is taken away by the pressure-induced removal of the encrustation.

Acknowledgments

The authors are grateful to Dr. Mohammad Athar and Dr. Xin Pei of Columbia University for the permission to access the chromameter and digital balance, respectively. The authors thank Mr. Justin Rasso for his technical assistance during the measurements.

References

[1] Asmus, J. F., Munk, W., and Murphy, C., 1974, "Studies on the Interaction of Laser Radiation With Art Artifacts," Proc. Soc. Photo-Opt. Instrum. Eng., **4**, pp. 19–27.
[2] Siano, S., Fabiani, F., Pini, R., Salimbeni, R., Giamello, M., and Sabatini, G., 2000a, "Determination of Damage Thresholds to Prevent Side Effects in Laser Cleaning of Pliocene Sandstone of Siena," J. Cultural Heritage, **1**, pp. s47–s53.
[3] Klein, S., Fekrsanati, F., Hildenhagen, J., Dickmann, K., Uphoff, H., Marakis, Y., and Zafiropulos, V., 2001, "Discoloration of Marble During Laser Cleaning by Nd:YAG Laser Wavelengths," Appl. Surf. Sci., **171**, pp. 242–251.
[4] Zhang, J., Birnbaum, A. J., Yao, Y. L., Xu, F., and Lombardi, J. R., 2007, "Effect of Fluence on the Discoloration of Marble Cleaned With UV Lasers," Appl. Surf. Sci., **253**(6), pp. 3083–3092.
[5] Kim, D., and Lee, J., 2004, "On the Physical Mechanism of Liquid-Assisted Laser Cleaning," J. Appl. Phys., **93**(1), pp. 762–764.
[6] Lu, Y. F., Song, W. D., Zhang, Y., and Low, T. S., 1998, "Theoretical Model and Experimental Study for Dry and Steam Laser Cleaning," Proc. SPIE, **3550**, pp. 7–18.
[7] Laboure, M., Bromblet, P., Orial, G., Wiedemann, G., and Simon-Boisson, C., 2000, "Assessment of Laser Cleaning Rate On Limestones and Sandstones," J. Cultural Heritage, **1**, pp. s21–s27.
[8] Siano, S., Fabiani, F., Caruso, D., Pini, R., and Salimbeni, R., 2000, "Laser Cleaning of Stones: Assessment of Operative Parameters, Damage Thresholds and Associated Optical Diagnostics," Proc. SPIE, **4070**, pp. 27–35.
[9] Cooper, M., Emmony, D., and Larson, J., 1995, "Characterization of Laser Cleaning of Limestone," Opt. Laser Technol., **27**, pp. 69–73.
[10] Thomas, G., 2002, "Thermal Properties of Gypsum Plasterboard at High Temperature," Fire Mater., **26**, pp. 37–45.
[11] Whitaker, S., 1977, "Simultaneous Heat, Mass and Momentum Transfer in Porous Media: A Theory of Drying," Adv. Heat Transfer, **13**, pp. 119–200.
[12] Ahmed, G., and Hurst, J., 1997, "Coupled Heat and Mass Transport Phenomena in Siliceous Aggregate Concrete Slabs Subjected to Fire," Fire Mater., **21**, pp. 161–168.
[13] Civan, F., and Sliepcevich, C. M., 1987, "Limitation in the Apparent Heat Capacity Formulation for Heat Transfer With Phase Changes," Proc. Okla. Acad. Sci., **67**, pp. 83–88.
[14] Wei, C. K., Davis, H. T., Davis, E. A., and Gordon, J., 1985, "Heat and Mass Transfer in Water-Laden Sandstone: Convective Heating," AIChE J., **31**(8), pp. 1338–1348.
[15] Bažant, Z. P., and Zi, G., 2003, "Decontamination of Radionuclides From Concrete by Microwave Heating. I: Theory," J. Eng. Mech., **129**(7), pp. 777–784.
[16] Ang, C. N., and Wang, Y. C., 2004, "The Effect of Water Movement on Specific Heat of Gypsum Plasterboard in Heat Transfer Analysis Under Natural Fire Exposure," Constr. Build. Mater., **18**, pp. 505–515.
[17] Li, L. Y., Purkiss, J. A., and Tenchev, R. T., 2002, "An Engineering Model for Coupled Heat and Mass Transfer Analysis in Heated Concrete," J. Mech. Eng. Sci., **26**, pp. 213–224.
[18] Edmondson, P. T., Grammatika, M., Fryer, P. J., and Handy, B., 2005, "Modelling of Heat Transfer, Mass Transfer and Flavor Development in Chocolate Crumb," *Seventh World Congress of Chemical Engineering*, Vol. 83, Issue No. 2, pp. 89–98.
[19] Reid, R., Prausnitz, J. M., Poling, B. E., 1987, *The Properties of Gases & Liquids*, McGraw-Hill Book Company, New York.
[20] Hearst, J. R., and Nelson, P. H., 1985, *Well Logging for Physical Properties*, McGraw-Hill, New York.
[21] Prencipe, M., Pascale, F., Zicovich-Wilson, C., Saunders, V., Orlando, R., and Dovesi, R., 2004, "The Vibrational Spectrum of Calcite (CaCO3): An Ab Initio Quantum-Mechanical Calculation," Phys. Chem. Miner., **31**, pp. 559–564.
[22] Faria, D., Silva, S., and Oliveira, M., 1997, "Raman Microspectroscopy of Some Iron Oxides and Oxyhydroxides," J. Raman Spectrosc., **28**, pp. 873–878.